Available online at www.sciencedirect.com
ScienceDirect
Atmospheric Environment 40 (2006) 6905–6917
ATMOSPHERIC ENVIRONMENT
www.elsevier.com/locate/atmosenv

Effects of particulate matter from gasoline and diesel vehicle exhaust emissions on silicate stones sulfation

J. Simão[a], E. Ruiz-Agudo[b], C. Rodriguez-Navarro[b,*]

[a]*Centro de Estudos Geológicos. Faculdade de Ciências e Tecnologia Universidade Nova de Lisboa, 2829-516 Caparica, Portugal*
[b]*Department of Mineralogia y Petrologia, Universidad de Granada Fuentenueva s/n, 18002 Granada, Spain*

Received 28 March 2006; received in revised form 12 June 2006; accepted 14 June 2006

Abstract

The effects of particulate matter (PM) from diesel and leaded gasoline motor vehicles exhaust emissions on sulfation of granites, syenite and gabbro stones have been experimentally studied. Abundant gypsum crystals and corrosion features developed on stones covered with diesel PM (DPM) following 72 h exposure to 100 ppm SO_2 at a relative humidity of 100%. In contrast, very small amounts of gypsum were observed on stones covered with gasoline PM (GPM), while no effect was observed on naked control stones. Abundant elemental C and Fe-rich particles in DPM play a critical role in the catalytic oxidation of SO_2 and the formation of H_2SO_4, which is responsible for silicate stone sulfation. Conversely, organic C and Pb-rich particles that are main components of GPM, do not play a significant role in sulfation. The response of each stone type towards sulfation is related to the stability of their constituent silicate minerals towards acid attack. Thus, the stones most susceptible to sulfation are those including nepheline (syenite), olivine, and pyroxene (gabbro), while granites in general, are most resistant to sulfation-related chemical weathering. These results help to explain how black (gypsum) crusts develop on silicate stones, and support limitations for (diesel) vehicular traffic and emission loads in urban centers.

Keywords: Black crusts; Gypsum; Silicate stones; Sulfation; C particles; Diesel PM

1. Introduction

Black crusts develop in rain-sheltered areas of stone buildings following acid deposition (dry deposition) of atmospheric pollutants (Rodriguez-Navarro and Sebastian, 1996). Their main component is gypsum ($CaSO_4 \cdot 2H_2O$), which is generally embedded in a mixture of pollution-derived particulate matter (PM), dust (e.g., carbonates, clay minerals and other silicates) and biogenic particles (e.g., pollen, bacteria and fungi) (Camuffo et al., 1982; Schiavon et al., 1995). Numerous analyses of sulfated building stones, as well as outdoor and laboratory exposure tests, have been performed as a first step to the design of means for preventing the detrimental effects of acid deposition on cultural heritage (e.g., Camuffo et al., 1982; Ross et al., 1989; Johnson et al., 1990; Sabbioni et al., 1996; Ausset et al., 1999). Zappia et al. (1993) have shown that, after sulfur, non-carbonate carbon is the main anthropogenic component of atmospheric

*Corresponding author. Fax: +34 958 243368.
E-mail address: carlosrn@ugr.es (C. Rodriguez-Navarro).

1352-2310/$ - see front matter © 2006 Elsevier Ltd. All rights reserved.
doi:10.1016/j.atmosenv.2006.06.016

deposition in gypsum crusts, and is responsible for their typical black color. Fossil-fuel combustion-derived PM and humidity have been shown to play an important role in the sulfation of carbonate stones (e.g., Cheng et al., 1987; Rodriguez-Navarro and Sebastian, 1996). PM appears to contribute to the catalytic oxidation of SO_2 to form SO_3, which in turn forms H_2SO_4 in the presence of humidity (Cheng et al., 1987; Ross et al., 1989). Dissolution of calcite ($CaCO_3$) and/or dolomite ($CaMg(CO_3)_2$) by H_2SO_4 leads to precipitation of gypsum and/or epsomite ($MgSO_4 \cdot 7H_2O$) (Tambe et al., 1991). Despite these observations, there is still some controversy as to the exact role played by PM in the sulfation of carbonate stone (Ausset et al., 1996, 1999; Johnson et al., 1996).

Although much progress has taken place in understanding carbonate stone sulfation, little is known about the sulfation of silicate stones (Haneef et al., 1993; Schiavon et al., 1995). Igneous silicate stones such as granites, andesite, basalt, tuff, trachyte, gabbro and syenite have been profusely used for building and decorative purposes since antiquity, and are also used as ornamental stones in modern buildings. The lack of experimental data regarding the effects of air pollution on silicate stones might be related to the assumption that such stones are not significantly affected by acid deposition because silicates are far less soluble at acid pH than carbonates. However, there are numerous examples of historical buildings made of granite (Smith et al., 1993; Schiavon et al., 1995; Grossi et al., 1998) or other igneous silicate stones such as andesite (Moropoulou et al., 2003) and trachyte (Mirwald et al., 1988), that show extensive development of black crusts in urban areas. How these black crusts develop is largely unknown. Furthermore, no research has yet clarified the role of vehicle exhaust PM in silicate stone sulfation.

Considering that motor vehicles are a principal source of urban air PM (Hildemann et al., 1994), here we have studied the sulfation of different silicate stones in the presence of diesel- and gasoline-powered motor vehicle exhaust PM. The aim of this work is to investigate the role played by diesel PM (DPM) and gasoline PM (GPM) in sulfation of granites, gabbro and syenite stones. We also attempt to characterize the size, morphology and composition of each type of PM, and to evaluate their relative contributions to the process of stone sulfation. By using different silicate stones with contrasting mineralogy, the responses to sulfation of each stone type, and each individual silicate mineral have been studied. Finally, since granites are the most common silicate building stone, the responses of four granites displaying differences in texture and degree of deuteric alteration (formation of secondary clay minerals) have been compared.

2. Materials and methods

2.1. Stones

Six silicate stones from Portugal were selected: four granites, one gabbro and one syenite. All of them have been used as building stones in the past and are currently quarried for similar purposes (Simão, 2003). Table 1 offers a detailed description of the mineralogical and petrographical characteristics of each stone type, as well as information on the extraction area and uses.

2.2. Collection and analysis of DPM and GPM

PM deposited on the inner wall of the exhaust tailpipe of light-duty vehicles using gasoline and diesel as fuels was collected using a brush. Shape, size and composition of collected GPM and DPM are similar to those of GPM and DPM collected on standard filters and/or transmission electron microscope (TEM) grids (see Section 3.1.). GPM was collected from noncatalyst leaded gasoline-powered vehicles 12–20 years old. Even though most vehicles use unleaded gasoline nowadays, leaded GPM was selected because black crusts in most historical buildings are currently highly enriched in Pb (Sabbioni and Zappia, 1992; Rodriguez-Navarro and Sebastian, 1996), an element which is mainly derived from leaded gasoline (Monna et al., 1997).

X-ray diffraction (XRD) analysis of PM was done on a Philips PW1710 diffractometer with Cu Kα radiation ($\lambda = 1.5405$ Å). Thermogravimetric (TG) analysis of PM was done on a Shimadzu TGA-50H coupled with Fourier transform infrared spectroscopy (FTIR; Nicolet 550) for evolved gas analysis. Analyses were performed in flowing air and at a constant heating rate of $10\,^{\circ}C\,min^{-1}$ (25–950 °C). FTIR analysis of PM was performed on a Nicolet IR200 using KBr pellets. The specific surface area of PM was determined by N_2 adsorption on a Micromeritics Tristar 3000. Prior to N_2 adsorption measurement, PM samples were heated at 110 °C for 2 h and outgassed to 10^{-3} Torr using a Micromeritics Flowprep. Morphology, size and

Table 1
Sources, texture and mineralogical–petrographic characteristics of tested silicate stones

Stone	Monção granite (MCG)	Vila real granite (VRG)	Castelo de vide granite (CVG)	Monforte granite (MFG)	Gabbro (GA)	Nepheline syenite (SY)
Source	Monção, Minho, NW Portugal	NE of Vila Real, Trás-os-Montes, NE Portugal	Cancho de S. Lourenço, Alto Alentejo, E Portugal	Maciço de Santa Eulália, Alto Alentejo, E Portugal	Castelo Ventoso, Odivelas, Alentejo, SE Portugal	Nave de Monchique, Algarve, S Portugal
Texture	Calc-alkaline, one mica, medium-coarse grained (aver. size: 4.3 ± 2.5 mm). Pink color.	Two mica, medium grained (aver. size: 2.8 ± 1.2 mm), intense feldspars deuteric alteration. Yellowish color.	Two mica, medium-coarse grained (aver. size: 4.6 ± 3.8 mm), extensive feldspar kaolinization. White color.	One mica, homogeneous, medium grained (aver. size: 2.5 ± 0.9 mm). Pinkish color.	Olivine-rich, medium grained (aver. size: 1.7 ± 1 mm). Dark color.	Medium to coarse grained (aver. size: 2.3 ± 1.6 mm) nepheline syenite. Gray color.
Main minerals	Quartz (25%), microcline (35%), plagioclase $An_{14.5}$ (27%), biotite (10%)	Quartz (27%), plagioclase An_{7-12} (26%), microcline (30%), biotite (6%), muscovite (10%)	Quartz (32%), microcline (36%), plagioclase An_{2-6} (16%), biotite (12%), muscovite (2%)	Quartz (22%) microcline (42%), plagioclase An_{3-6} (18%), biotite (13%)	Plagiclase (labradoorite) An_{59-63} (66%), pyroxene (augite) (24%), olivine Fa_{28} (8%)	Ortoclase (45%), albite (2%), nepheline (22%), aegirine–augite (10%), titanite (8%), biotite (6%)
Accessory minerals	Muscovite, titanite, zircon, apatite, allanite, hornblende, Fe oxides (up to 3%)	Zircon, apatite, Fe oxides, tourmaline, rutile, Al silicates, cordierite, chlorite, kaolinite, calcite (up to 1%)	Apatite, titanite, zircon, tourmaline, rutile, kaolinite, sericite, chlorite, Fe oxides (up to 2%)	Titanite, zircon, hornblende, allanite, chlorite, muscovite, Fe oxides (up to 5%)	Biotite, hornblende, serpentine, Fe oxides (up to 2%)	Sodalite, cancrinite, apatite, hornblende, rutile, zircon, Fe oxides, kaolinite, zeolites, muscovite, calcite (up to 7%)
Examples of uses	Matriz Church, Monção, Portugal	S. Domingo Church, Vila Real, Portugal	Castelo (XIII c.), Sintra; Santa Maria Church, Castelo da Vide, Portugal	Elisabeth Towers, Dubai, UAE; Sony City, Amsterdam, The Netherlands	Ministério da Saúde, Lisboa, Portugal	Universidade Nova da Lisboa, Portugal; Great Northern Sq., Manchester, UK

composition of PM were studied with a Philips CM20 analytical TEM operated at 200 kV and equipped with an energy dispersive X-ray spectrometer (EDS). Prior to TEM analysis, particles were dispersed in ethanol, sonicated for 30 s, and placed on Formvar© C-coated Cu grids.

2.3. Experimental SO_2 attack

Sulfation tests were performed in a Kesternich SO_2 static chamber. The chamber and experimental conditions have been described elsewhere (Rodriguez-Navarro and Sebastian, 1996). SO_2 was dosed at the beginning of the test at a concentration of 100 ppm. Note that such SO_2 concentration is ~2000 times higher than current SO_2 levels in most urban areas (Rodriguez-Navarro and Sebastian, 1996; Ausset et al., 1999). However, since one of the main goals of the experiment was to demonstrate that PM enhances stone sulfation, we chose to use this high concentration in order to obtain a high reaction rate.

Prior to SO_2 exposure, stone samples were cut in $5\times5\times1$ cm slabs using a diamond saw. The average grain size of the tested stones is 3.1 ± 1.8 mm (see details in Table 1). Thus, an average of ~330 mineral grains per sample largest face were exposed to SO_2 attach. The selected sample size was therefore considered large enough to yield representative results. The upper largest

face was polished (i.e., mimicking natural stone industry surface finishing) to facilitate identification of surface dissolution/corrosion features developed following SO_2 exposure. PM was evenly sprinkled over the polished upper surface of each stone type as in Ausset et al. (1999). Three samples of each stone type (a total of 18 samples) were introduced in the chamber before SO_2 dosage: (a) a control (no PM coating); (b) a sample coated with $4\,mg\,cm^{-2}$ GPM; and (c) a sample coated with $4\,mg\,cm^{-2}$ DPM. Chamber temperature was set at 25 °C, samples were placed on dampened cellulose paper, and a container full of water was placed at the bottom of the chamber. A relative humidity (RH) of ~100% was thus reached. This simulates a frequently occurring outdoor condition, where stones are coated with a thin film of condensed moisture (Tambe et al., 1991). It has been pointed out that a high RH accelerates sulfate attack by SO_2 dry deposition (Johnson et al., 1990). After 72 h SO_2 exposure, samples were withdrawn from the chamber and their surfaces were studied with a Zeiss DSM950 scanning electron microscope (SEM) coupled with an EDS detector. Samples were carbon-coated prior to SEM-EDS analysis.

3. Results and discussion

3.1. Analysis of PM

XRD patterns of DPM and GPM showed a broad hump at 20–30 °2θ due to the presence of poorly crystalline (or amorphous) solids (Fig. 1). In addition, DPM showed small Bragg peaks corresponding to graphite ($d_{002} = 0.34$ nm). Poorly crystalline pregraphitic carbons (cokes and pitches) and graphite are main components of DPM (Babu et al., 1995). Small Bragg peaks corresponding to anhydrite ($CaSO_4$) were also detected. Anhydrite presence is consistent with the reported S and Ca content (2.4 and 0.74 wt%, respectively) of the tested DPM (Rodriguez-Navarro and Sebastian, 1996). Note that calcium sulfate is a common component of DPM, and is thought to form following oxidation and hydrolysis of S in diesel vehicles exhaust systems (Kittelson, 1998) and reaction with Ca from lubricating oil combustion (Cadle et al., 1999). Besides poorly crystalline material, GPM contained lead bromide oxide ($Pb_8O_7Br_2$), and magnetoplumbite ($PbFe_{12}O_{19}$). Anglesite ($PbSO_4$) was also detected. Its presence is consistent with S content of 1.67 wt% in GPM

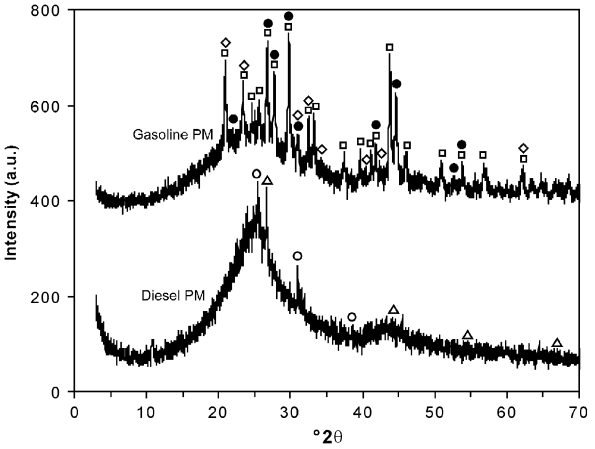

Fig. 1. XRD patterns of GPM and DPM. Bragg peaks of graphite (△), anhydrite (○), magnetoplumbite (◇), lead sulfate (□) and lead oxide bromide (●) are indicated.

(determined on a Fisons Carlo Erba EA 1108 elemental analyzer).

TG coupled with FTIR analysis of evolved gases showed that the evaporative component was 91.8 and 81.2 wt% in DPM and GPM, respectively (Fig. 2a). The residual non-evaporative fraction is assumed to be ashes (oxides, silicates and sulfates, as indicated by XRD and TEM analyses). Detection of CO_2, CO and H_2O by FTIR (Fig. 2b and c) suggests that the evaporative fraction included organic carbon (OC) and elemental carbon (EC). Trace amounts of SO_2 were evolved from DPM over a temperature (T) range 400–500 °C, while higher amounts of SO_2 were evolved from GPM over a T range 300–450 °C. Such relatively low decomposition T suggests that SO_2 originates from organics or adsorbed SO_2, because decomposition of sulfates occurs at higher T (MacKenzie, 1970). C decomposition (oxidation) took place over a T range 110–500 and 140–700 °C, in the case of GPM and DPM, respectively. Decomposition rates were higher in GPM than in DPM. In addition to CO_2, CO, H_2O and SO_2, GPM evolved other gaseous organic compounds (Fig. 2b). Infrared absorption bands of polycyclic aromatic hydrocarbons (PAHs; e.g., anthracene and/or phenantrene) were detected. These results suggest that OC is a principal component of GPM. Note that OC typically decomposes in air at lower T than EC (MacKenzie, 1970; Nguyen et al., 2004). Although it has been reported that OC in PM can be removed by heating in air at 450 °C (Zinbo et al., 1993), no attempt was made to quantify total OC and EC based on TG

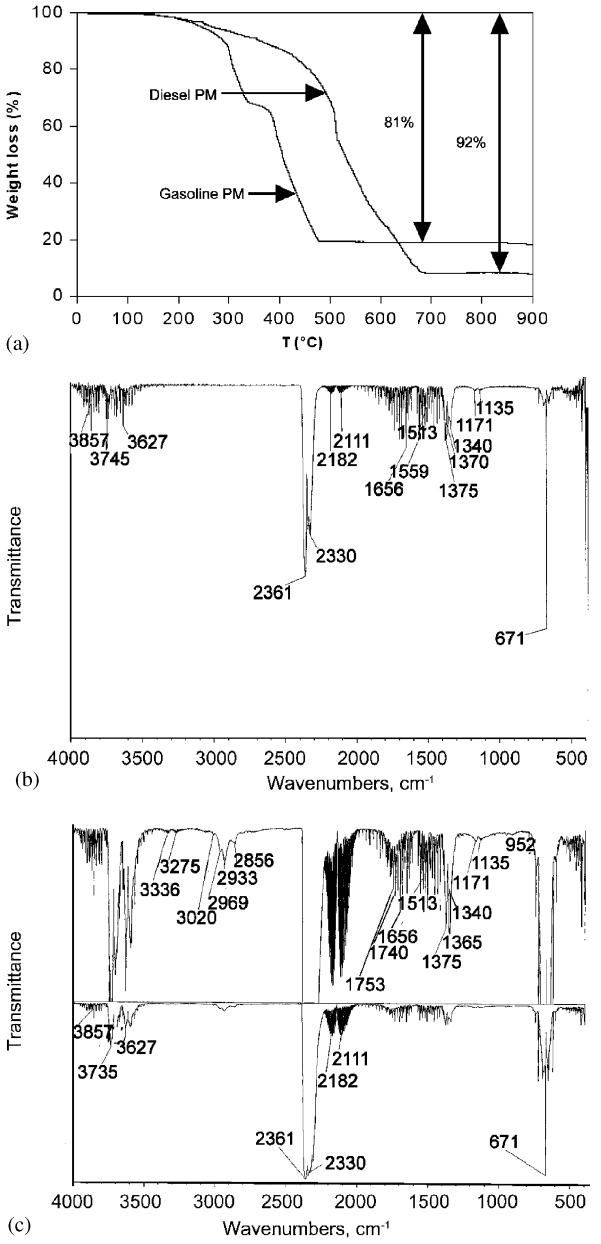

Fig. 2. TG-FTIR analysis of GPM and DPM: (a) TG curves of GPM and DPM; (b) DPM and (c) GPM evolved gas FTIR spectra showing main absorption bands of H_2O (3857, 3745, 1656, 1559, 1513 cm^{-1}), CO_2 (3735, 3627, 2361, 2330, 671 cm^{-1}), CO (2182, 2111 cm^{-1}), SO_2 (1375, 1370 cm^{-1}) and PAHs (3336-2856 cm^{-1}) (Colthup et al., 1990). GPM full FTIR spectrum (bottom) as well as a detail (top) are shown in (c).

results since charring may lead to erroneous quantification (Nguyen et al., 2004). TG analysis of DPM showed that significant amounts of C were decomposed at $T > 500\,^{\circ}C$. This high decomposition T confirms that EC is the main component of DPM

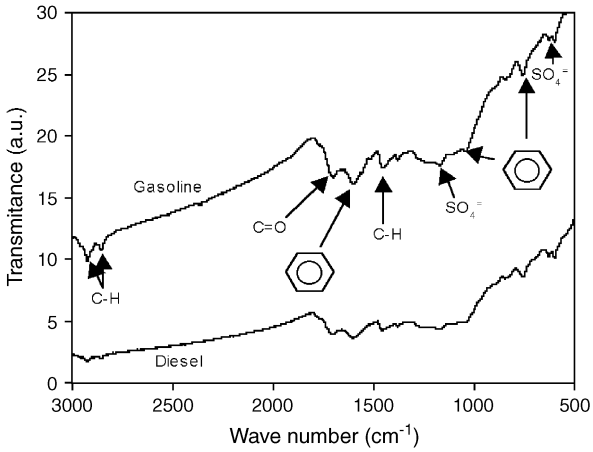

Fig. 3. FTIR spectra of GPM and DPM. Main absorption bands (and corresponding bonds) are indicated.

(Kittelson, 1998). These results are consistent with the reported high concentration of OC (mainly PAHs) in GPM from vehicles lacking catalytic converters (Hildemann et al., 1991). Hildemann et al. (1991) have reported that particles emitted by non-catalyst- and catalyst-equipped gasoline-powered vehicles are largely composed by OC, while particles emitted from diesel engines contain significantly higher amounts of EC.

FTIR spectra of GPM and DPM were very similar (Fig. 3). Presence of sulfates was confirmed by the out-of-phase $SO_4^{=}$ stretch at 1190 cm^{-1} and bending bands at around 630 cm^{-1}. Hydrocarbons were also present in both GPM and DPM: (C–H asymmetric stretch at 2940 cm^{-1}; C–H symmetric stretch at 2870 cm^{-1}; C–H asymmetric bending at 1460 cm^{-1}; and C–H symmetric bending at 1380 cm^{-1}), together with aromatic compounds (C–C aromatic skeletal stretching around 1620 cm^{-1}, and C–H out of plane bending at 770 cm^{-1}). However, the aromatic C–H stretch was not observed most probably due to the strong absorption of the samples at high wavenumbers. Nonetheless, the C = O absorption band at 1720 cm^{-1} was observed, thus confirming the presence of carbonyl compounds (Colthup et al., 1990). Kittelson (1998) has reported that diesel and gasoline C particles are typically surrounded by adsorbed PAHs, an observation consistent with our FTIR results. Absorption bands of sulfates and organic compounds were better defined in GPM than in DPM. This is related to their greater abundance in GPM as indicated by TG-FTIR and XRD results.

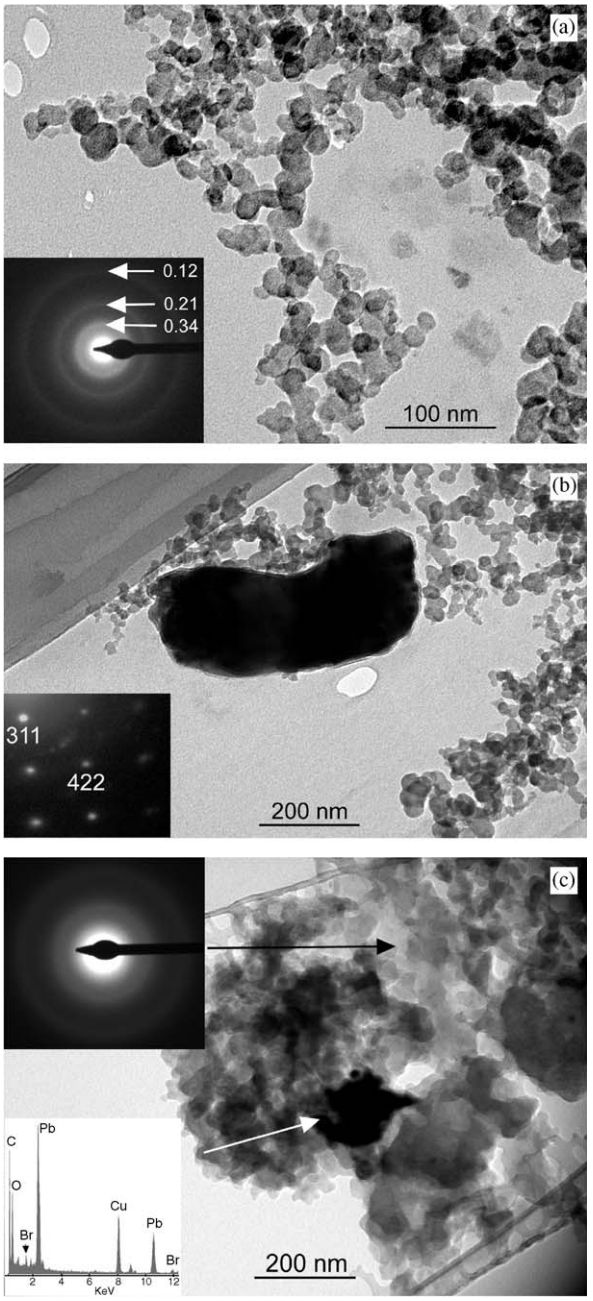

Fig. 4. TEM photomicrographs of: (a) fractal aggregate of diesel C particles. The SAED (inset) shows diffuse rings at d-spacings (in nm) corresponding to graphite; (b) detail of Fe-rich particle in DPM. Its SAED pattern (inset) shows diffraction spots corresponding to (311) and (422) planes of magnetite; and (c) gasoline poorly crystalline C particles (see diffuse halos in SAED pattern in inset) and Pb–Br-rich particles (see EDS spectrum in inset).

TEM-EDS analyses confirmed that C particles are main components in both DPM and GPM. C particles in DPM (Fig. 4a and b) were smaller (mean size 30 ± 15 nm) than those in GPM (30–200 nm) (Fig. 4c). Diesel C nanoparticles formed open chain-like fractal aggregates, similar to those described by Katrinak et al. (1993). Gasoline C aggregates were more compact. Note, however, that TEM sample preparation may have altered the original fractal structure (and fractal dimension) of the aggregates. C particles were randomly oriented and poorly crystalline as shown by the diffuse rings in SAED patterns (see insets in Fig. 4a and c). Nonetheless, SAED rings at 0.34, 0.21 and 0.12 nm corresponding to graphite, were detected in DPM (inset in Fig. 4a). Similar SAED features of diesel C particles have been reported (e.g., Murr and Bang, 2003). Scarce Fe particles, which are magnetite (Fe_3O_4) as shown by SAED (inset in Fig. 4b), were also observed in DPM (Fig. 4b). Abdul-Razzak and Gautam (2001) have reported magnetite presence in DPM, while it has been found by Schiavon and Zhou (1996) in black crusts on historical monuments. Gasoline non-C particles, that were present in significant amounts, included: (a) large (up to 0.5 μm), abundant Pb–Br-rich particles (Fig. 4c). Their SAED pattern indicates that they are lead oxide bromide, in agreement with XRD results. The presence of this Pb–Br phase in GPM is explained by the thorough use of $Pb(C_2H_5)_4$ and $C_2H_4Br_2$ as additives in leaded gasoline (Rodriguez-Navarro and Sebastian, 1996); (b) Pb–S-rich particles. Their SAED pattern shows that they are $PbSO_4$, an observation consistent with XRD results. Similar $PbSO_4$ particles have been found in polluted urban air (Xie et al., 2005); (c) Fe-rich particles that included minor amounts of Pb, and trace amounts of Zn and Ni. They were crystalline, but their SEAD pattern could not be properly resolved. It is assumed that they are magnetoplumbite (see XRD analysis); (d) Si–Al-rich particles with trace amounts of K, Mg and S. Their SAED pattern was masked by the diffuse electron diffraction rings of C particles. We assume that they are aluminosilicates, although the exact phase(s) could not be identified.

Particles (b)–(d) have sizes ranging from 50 to 200 nm. The observed metallic-rich particles are typical of GPM and DPM (Rodriguez-Navarro and Sebastian, 1996).

The specific surface area of DPM was $83.9 \pm 0.9\ m^2\ g^{-1}$, while that of GPM was $5.75 \pm 0.03\ m^2\ g^{-1}$. These results are consistent with the presence of a significant amount of C nanoparticles in DPM, and are in good agreement with the values

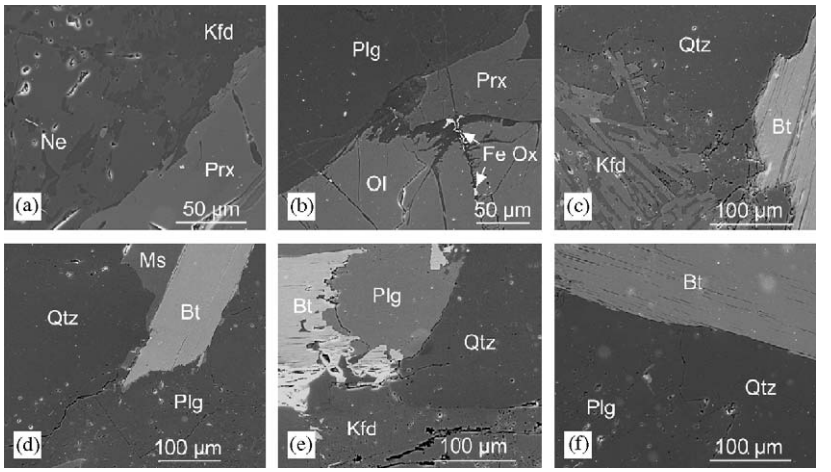

Fig. 5. SEM photomicrographs of control samples: (a) syenite (Ne: nepheline; Prx: pyroxene; Kfd: K feldspar); (b) gabbro (Plg: plagioclase; Ol: olivine). Iron oxides (FeOx) in Ol fractures were originally present before testing; (c) VRG granite (Bt: biotite; Qtz: quartz). Note small pits in alkali feldspars are due to deutheric alteration; (d) CVG granite (Ms: muscovite); (e) MCG granite; and (f) MFG granite.

reported in the literature (Nguyen et al., 2004). A smaller surface area of GPM is consistent with the larger size, lower abundance, and high degree of agglomeration of its C particles. However, the observed sizes of C particles in GPM (TEM results) are not fully consistent with such a relatively low surface area. This apparent inconsistency can be explained by considering that the high molecular weight of Pb compounds in GPM significantly reduces the volume of ultrafine C particles per unit mass.

3.2. Experimental sulfation of silicate stones

In all cases, control samples exposed to SO_2 in the Kesternich chamber neither showed sign of decay of their constituent minerals, nor formation of any secondary minerals (i.e., sulfates) (Fig. 5). Conversely, weathering (dissolution/etching) features on silicate crystals, as well as newly formed phases, were observed on the surface of samples covered with PM and exposed to SO_2 and humidity. One of the most affected stones was the syenite. In the presence of DPM, formation of gypsum crystals associated to C (and Fe-rich) particles was systematically observed on nepheline ($KNa_3Al_4\ Si_4O_{16}$) (Fig. 6a and b), on alkali feldspars ($(K,Na)AlSi_3O_8$), and on etched aegirine–augite pyroxene ($(Ca,Na)(Mg,\ Fe^{2+},Fe^{3+})[Si_2O_6]$) crystals (Fig. 6c). Newly formed halite (NaCl) and thenardite (Na_2SO_4), presumably mirabilite ($Na_2SO_4 \cdot 10H_2O$) that underwent dehydration (Ausset et al., 1999), were also observed on weathered nepheline crystals (Fig. 6d–f), along with euhedral gypsum crystals developed on DPM aggregates (Fig. 6g). Weathered nepheline grains showed a microcracked film of silica gel (Fig. 6d). Tole et al. (1986) have reported acid dissolution of nepheline via formation of a superficial aluminosilicate amorphous gel, which shrinks and cracks upon drying, as observed here. Gypsum formation is ascribed to $SO_4^{=}$ bonding to Ca^{2+} released upon acid dissolution of aegirine-augite and titanite ($CaTiSiO_5$), i.e., the only Ca-bearing silicates in this stone. Similarly, Na_2SO_4 appears to form after acid lixiviation of Na^+ from nepheline. The formation of halite is consistent with dissolution and release of Na^+ and Cl^- from nepheline and accessory minerals such as sodalite ($Na_8Al_6Si_6O_{24}Cl_2$) and cancrinite ($Na_6Ca_2Al_6Si_6O_{24}(CO_3,SO_4,Cl)_2 \cdot nH_2O$). GPM induces little weathering on the syenite minerals. Nonetheless, small amounts of gypsum and halite were formed, while etching was observed in pyroxene grains. Although chemical weathering appears to be dominant in this stone type, eventual salt weathering phenomena associated to crystallization of sodium chloride and sodium sulfates (Rodriguez-Navarro and Doehne, 1999) can not be ruled out.

The gabbro was also highly susceptible to sulfation. Gypsum formation was observed on weathered plagioclase ($(Ca,Na)(Al,Si)_4O_8$) grains covered by DPM (Fig. 7a). Acid dissolution of

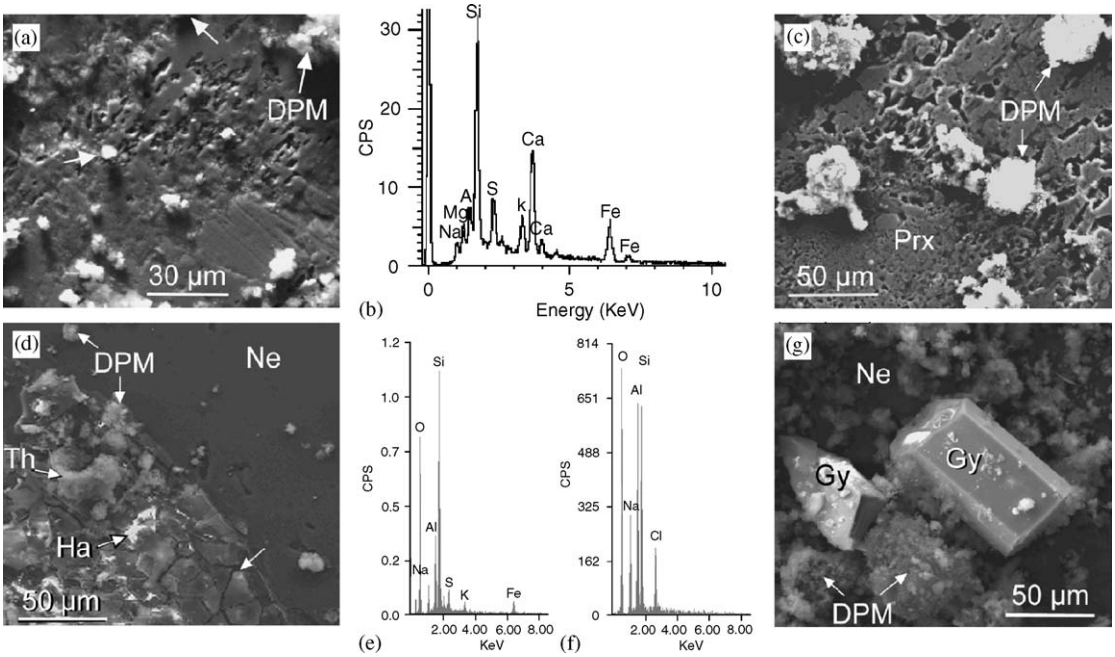

Fig. 6. SEM photomicrographs of syenite stone after SO_2 exposure: (a) etched nepheline (Ne) crystal with DPM and gypsum (Gy) crystals (arrows) on its surface; (b) EDS spectrum of Gy crystal in (a); (c) corroded pyroxene (Prx) covered with DPM; (d) Ne crystal with a cracked surface (arrow) and newly formed thenardite (Th) and halite (Ha); (e) EDS spectrum of Th in (d); (f) EDS spectrum of Ha in (d): and (g) large, euhedral Gy crystals on Ne associated to DPM.

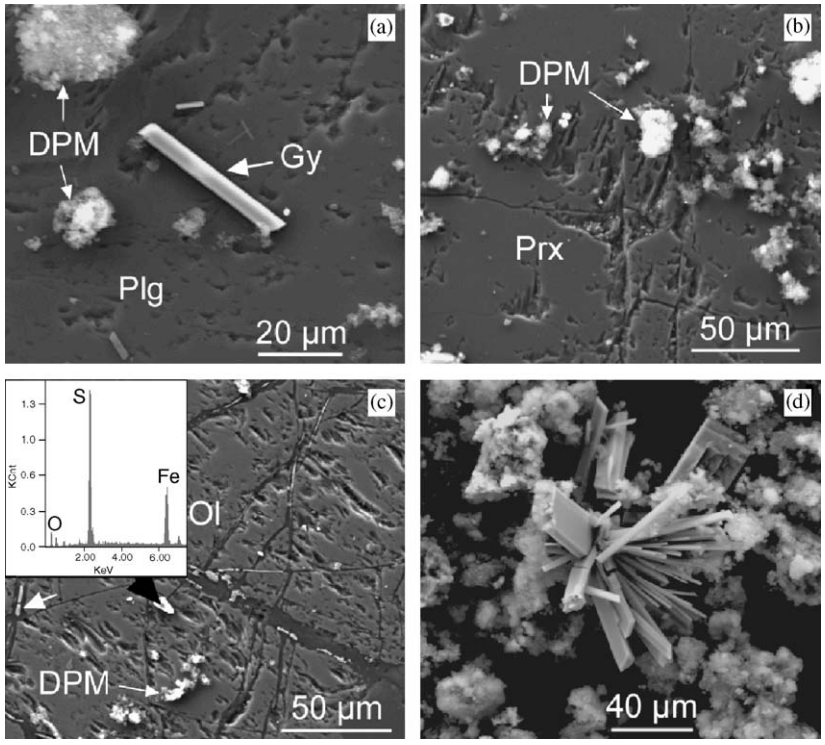

Fig. 7. SEM photomicrographs of gabbro stone after SO_2 exposure: (a) acicular gypsum (Gy) on plagioclase (Plg) crystal. DPM is also observed; (b) etched pyroxene (Prx) crystal covered with DPM; (c) olivine (Ol) crystal showing extensive corrosion along cracks and formation of iron sulfate (EDS spectrum in inset) in the presence of DPM. Deepening of crevices containing iron oxide (white arrow) is observed; and (d) Gy aggregates on plagioclase covered with DPM.

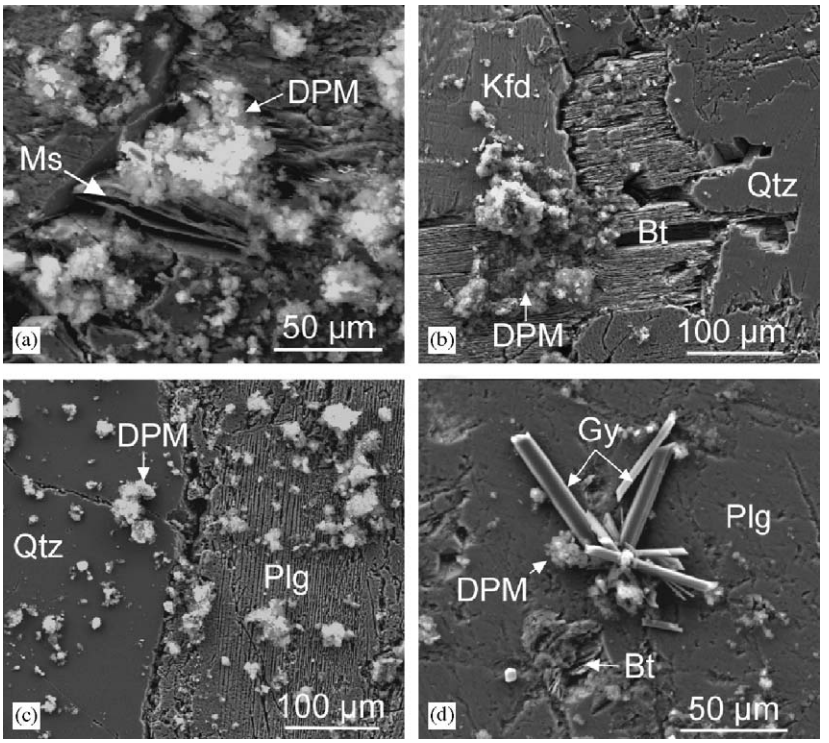

Fig. 8. SEM photomicrographs of granite stones after SO_2 exposure: (a) muscovite in VRG stone showing opening of basal planes associated to DPM; (b) biotite (Bt) basal planes opening and loss of material in contact with K feldspar (Kfd) and quartz (Qtz) in CVG stone; (c) CVG stone showing corrosion features in plagioclase (Plg) covered with DPM; and (d) MCG stone showing gypsum (Gy) aggregates formed on Plg, associated to DPM and weathered Bt.

Ca-rich plagioclase results in Ca release, which in the presence of sulfates precipitates as gypsum. Note that Ca-rich plagioclase (i.e., the labradorite in this gabbro) is less resistant to acid dissolution than Na-rich plagioclase (e.g., albite and oligoclase in granites) (Wilson 2004). DPM was also associated to corrosion features along cleavage planes of augite pyroxene ($Ca(Mg, Fe)(Si, Al)_2O_6$) (Fig. 7b), and along cracks in olivine ($(Mg,Fe)_2SiO_4$) crystals. Olivine crystals developed iron sulfate crystals on their etched surface (Fig. 7c). Isolated euhedral gypsum crystals with a radial arrangement formed on DPM agglomerates placed on plagioclase crystals (Fig. 7d). In the presence of GPM, poorly developed corrosion features were observed on pyroxene and olivine grains associated to a few gypsum crystals. Wilson (2004) indicates that acid dissolution of olivine is very rapid and results in the release of Fe and to a lesser extent Mg, followed by formation of a superficial Fe-depleted, silica-rich surface layer. Fe release explains the formation of iron sulfates upon SO_2 attack. However, note that olivine cracks filed with Fe oxides were present in the original gabbro (Fig. 5b). Thus, Fe sulfate may have preferentially formed upon acid attack of such cracked areas. Pyroxenes rank third to olivine and Ca-plagioclase in susceptibility to acid attack that results in etching along cleavage planes. Deeply etched cleavage planes are typical features of acid dissolved pyroxenes (Wilson, 2004). Simão (2003) studied the effects of diluted solutions of HCl, HNO_3 and H_2SO_4 (simulating acid rain) on gabbro stones. The main components, plagioclase and olivine, both responded in similar ways to each acid solution, although following different trends. While plagioclase developed a thin surface layer of microcracked silica gel, which protected the underlying mineral, olivine initially underwent alteration due to leaching of magnesium and iron and, in a following stage, was (mechanically) removed from the rock.

Regarding the granites: (a) VRG showed very small amounts of gypsum around DPM deposited on biotite ($K(Mg,Fe)_3AlSi_3O_{10}(OH,F)_2$). Ca for

gypsum formation appears to come from dissolution of plagioclase ($Na_{0.88}Ca_{0.12}Al_{1.12}Si_{2.88}O_8$). Dissolution and corrosion effects resulting in open cleavage planes were observed in muscovite ($KAl_2(Si_3Al)O_{10}(OH,F)_2$) (Fig. 8a) and biotite mica crystals; (b) CVG showed very limited new formation of gypsum crystals on DPM deposited over biotite. The latter displayed opening of cleavage planes. Loss of material was most evident at biotite/quartz (SiO_2) and K feldspar/biotite grain boundaries (Fig. 8b). Biotite and muscovite acid dissolution occurs primarily via release of interlayer K, followed by octahedral Fe oxidation in the case of biotite (Wilson, 2004). K release results in the opening of cleavage planes, as depicted in our SEM photomicrographs. Some dissolution (corrosion) features were observed on alkali feldspar grains that showed new formation of micron-sized secondary aluminosilicates, most probably clay minerals (Fig. 8c). This observation is consistent with the reported dissolution and kaolinization of feldspars in granite stone via heterogeneous attack of a mixture of $SO_{2(gas)}$ and $H_2O_{(vapor)}$ (Schiavon, 2000). The plagioclase ($Na_{0.94}Ca_{0.06}Al_{1.06}Si_{2.94}O_8$) is the only (limited) Ca source for gypsum formation on CGV; (c) MCG showed scarce, well developed gypsum crystals associated to both DPM and GPM. The best development of gypsum was observed on biotite and plagioclase crystals covered by DPM (Fig. 8d). Smith and Magee (1990) and Smith et al. (1993) have shown similar gypsum crystals associated to PM on granite surfaces weathered in an urban environment; (d) MFG is the stone less susceptible to decay by sulfation in the presence of PM. We only detected the formation of scarce isolated gypsum crystals associated to DPM.

VRG and CVG are the granites most affected by sulfation, i.e., they show the highest development of gypsum and corrosion features. Interestingly, these two granites are the only ones that display deuteric alteration and kaolinization of the alkali feldspars. Along with quartz, alkali feldspars (Na plagioclase and K feldspar) are among the most acid resistant silicates (Wilson, 2004). This explains why they generally show very little decay upon SO_2 attack. Wilson (2004) reports that deuteric/hydrothermal alteration promotes feldspar dissolution under acid conditions, as has also been observed in the present work.

The differential response of each stone type towards sulfation is related to the stability towards acid dissolution of its rock-forming silicate minerals. Franke and Teschner-Steinhardt (1994) have shown that the stability towards chemical weathering (acid dissolution) of silicate minerals decreases in the order muscovite-alkali feldspar-biotite-pyroxene-Ca plagioclase-nepheline-olivine. Thus, the most acid resistant minerals are those present in granites, while the less resistant are those in the gabbro and the syenite stones. Thus, according to the ease of sulfation in the presence of PM, the stones rank as follows: syenite $\geqslant$ gabbro $\ggg$ granites.

3.3. The role of PM on silicate stone sulfation

The development of corrosion features and sulfates on samples in which DPM, and to a lesser extent GPM, were deposited, as well as the lack of corrosion or sulfate formation on control samples exposed to SO_2, suggest that PM plays a critical role on silicate stone sulfation. These results show that oxidation of SO_2 in a heterogeneous phase onto solid surfaces in the presence of carbonaceous (and metallic-rich) particle catalyzers and humidity has taken place (Rodriguez-Navarro and Sebastian, 1996). Catalytic oxidation of SO_2 in the presence of metal (e.g., Fe, V, Zn or Ni) and oxide PM, as well as carbonaceous PM emitted by a range of sources, e.g., power plants, stoves, vehicles and heating systems, has been demonstrated (see Rodriguez-Navarro and Sebastian, 1996, and references therein). In particular, EC particles, which are the main component of DPM, play a crucial role in the catalytic oxidation of SO_2 (Novakov et al., 1974), leading to the formation of sulfuric acid in the presence of humidity (Ross et al., 1989).

Sulfuric acid attack of silicate phases resulted in the observed corrosion/dissolution features of mineral grains, and in the eventual formation of sulfates (mainly gypsum). The higher effectiveness of DPM on the corrosion and sulfation of silicate stones when compared with GPM, is consistent with the higher amount of EC particles in the former, as evidenced by XRD, TG-FTIR and TEM-EDS/SAED analyses. The ultrafine size of such EC particles appears to further promote sulfation of silicate stones, since such nanoparticles display a high surface area (N_2 adsorption results), and are thus highly reactive. However, the role of metal-rich particles (specially Fe-rich particles) should not be overlooked (Brimblecombe and Speeding, 1974; Sabbioni et al., 1996; Schiavon and Zhou, 1996), since they are also efficient catalyzers for SO_2 oxidation, as previously stated.

Our results show that EC particles from diesel motor vehicle exhaust play a crucial role on silicate stone sulfation. A similar effect has been found in the case of carbonate stone (Rodriguez-Navarro and Sebastian, 1996). In contrast, Johnson et al. (1996) and Ausset et al. (1996) have reported a negligible effect of DPM on limestone and sandstone sulfation. However, in both cases a mixture of NO_2 and SO_2 was used during dry deposition sulfation tests performed at RH < 84%. On the one hand, the presence of NO_2, a well-known catalyst for SO_2 oxidation, could have masked any catalytic effect of DPM. On the other hand, the absence of condensation might explain the low SO_2 fixation rates observed in both naked and DPM covered samples. In any case, the low sulfation level observed by these authors makes very difficult to draw any conclusion about the role (positive or otherwise) of DPM on stone sulfation. Conversely, it could be argued that our results might be biased by the high concentration of SO_2 we have used. However, the used SO_2 concentration does not seem to affect sulfation dynamics. It only appears to have a direct effect on the kinetics of sulfation. This is consistent with the absence of sulfates or corrosion features on naked stone, and their fast development (within 3 days) on the PM-covered stones. However, one should expect a less dramatic effect in real case scenarios, an effect which could be evaluated by outdoor exposure testing of DPM- and GPM-covered stone samples.

Regarding the impact of DPM on architectural heritage, it should be noted that urban PM typically contains a significant fraction (>14%) of diesel carbonaceous particles, which are primary contributor for EC (Hildemann et al., 1994). For instance, on-road diesel combustion in the UK is thought to contribute between 80% and 95% of airborne EC level (Colebeck, 1995). These data clearly emphasize the significant role diesel carbonaceous PM (EC in particular) plays in current urban air pollution. In addition, ultrafine diesel C particles appear to have important adverse effects on human health (Murr and Bang, 2003). Thus, measures aimed at limiting motor vehicle traffic and exhaust emissions within historical centers, as well as those striving to reduce carbon PM emission loads from combustion of fossil fuels, diesel in particular, could be highly beneficial both for humans and for built heritage.

Finally, there are two aspect connected with the effects of vehicle PM emissions that deserve future research. On the one hand, Mitchell and Gu (2000) have reported that hydrocarbon consuming bacteria enhance acid-related biodeterioration of stone. Although we observed no microbial growth in our test, most probably due to its short duration, it would be worth to test the effects of OC present in DPM and GPM on biodeterioration, which has been suggested to be important in granite stone decay (Schiavon et al., 1995). On the other hand, and considering that leaded gasoline is being phased out worldwide, future research should involve an evaluation of the effects of unleaded GPM on stone sulfation. This is of particular interest because unleaded GPM emitted by catalyst autos has a higher concentration of ultrafine EC than leaded GPM emitted by non-catalyst autos (Hildemann et al., 1991).

Acknowledgments

The authors are grateful to Prof. Zenaide Silva, Principal Investigator and Coordinator of the Project CTM/10067/1998—PRAXIS XXI, financially sponsored by Fundação para a Ciência e a Tecnologia, Portugal. This research has been also financially supported by MCYT (Spain) under contract MAT2003-02723, and Junta de Andalucía Research Group RNM-179. We thank the personnel of the CIC (Universidad de Granada), and CEAMA (Junta de Andalucía) for their help during TG-FTIR, SEM, and TEM analyses. Editing of the original English manuscript was done by M. Bettini.

References

Abdul-Razzaq, W., Gautam, M., 2001. Discovery of magnetite in the exhausted material from a diesel engine. Applied Physics Letter 78, 2018–2019.

Ausset, P., Crovisier, J.L., Del Monte, M., Furlan, V., Girardet, F., Hammecker, C., Jeannette, D., Lefevre, R.A., 1996. Experimental study of limestone and sandstone sulphation in polluted realistic conditions: the Lausanne atmospheric simulation chamber (LASC). Atmospheric Environment 30, 3179–3207.

Ausset, P., Del Monte, M., Lefevre, R.A., 1999. Embryonic sulphated black crusts on carbonate rocks in atmospheric simulation chamber and in the field: role of carbonaceous fly ash. Atmospheric Environment 33, 1525–1534.

Babu, B.S., Farinash, L., Seehra, M.S., 1995. Carbons in diesel particulate matter: structure, microwave-absorption, and oxidation. Journal of Materials Research 10, 1075–1078.

Brimblecombe, P., Speeding, D.J., 1974. The catalytic oxidation of micromolar aqueous sulphur dioxide-1. Oxidation in dilute solutions containing iron (III). Atmospheric Environment 8, 937–945.

Cadle, S.H., Mulawa, P.A., Hunsanger, E.C., Nelson, K., Ragazzi, R.A., Barrett, R., Gallagher, G.L., Lawson, D.R., Knapp, K.T., Snow, R., 1999. Composition of light-duty motor vehicle exhaust particulate matter in the Denver, Colorado area. Environmental Science and Technology 33, 2328–2339.

Camuffo, D., Del Monte, M., Sabbioni, C., Vittori, O., 1982. Wetting, deterioration and visual features of stone surfaces in an urban area. Atmospheric Environment 16, 2253–2259.

Cheng, R.J., Hwu, J.R., Kim, J.T., Leu, S.M., 1987. Deterioration of marble structures: the role of acid rain. Analytical Chemistry 59, 104A–106A.

Colebeck, I., 1995. Particle emission from outdoor and indoor sources. In: Kouimtzis, T., Somaria, C. (Eds.), Airborne Particulate Matter. Springer, Berlin, pp. 1–35.

Colthup, N.B., Daly, L.H., Wiberley, S.E., 1990. Introduction to Infrared and Raman Spectroscopy, third ed. Academic Press, New York.

Franke, W.A., Teschner-Steinhardt, R., 1994. An experimental approach to the sequence of the stability of rock-forming minerals towards chemical weathering. Catena 21, 279–290.

Grossi, C.M., Esbert, R.M., Diaz-Pache, F., 1998. Decay and durability of building stones in urban environments. Materiales de Construcción 48, 5–25.

Haneef, S.J., Johnson, J.B., Jones, M., Thompson, G.E., Wood, G.C., Azzaz, S.A., 1993. A laboratory simulation of degradation of Leinster granite by dry and wet deposition processes. Corrosion Science 34, 511–524.

Hildemann, L.M., Markowski, G.R., Ross, G.R., 1991. Chemical composition of emissions from urban sources of fine organic aerosol. Environmental Science and Technology 25, 744–759.

Hildemann, L.M., Klinedinst, D.B., Klouda, G.A., Currie, L.A., Cass, G.R., 1994. Sources of contemporary carbon aerosol. Environmental Science and Technology 28, 1565–1576.

Johnson, J.B., Haneef, S.J., Hepburn, B.J., Hutchinson, A.J., Thompson, G.E., Wood, G.C., 1990. Laboratory exposure systems to simulate atmospheric degradation of building stone under dry and wet deposition conditions. Atmospheric Environment 24A, 2585–2592.

Johnson, J.B., Montgomery, M., Thompson, G.E., Wood, G.C., Sage, P.W., Cooke, M.J., 1996. The influence of combustion-derived pollutants on limestone deterioration: 1. The dry deposition of pollutant gases. Corrosion Science 38, 105–131.

Katrinak, K.A., Rez, P., Perkes, P.R., Buseck, P.R., 1993. Fractal geometry of carbonaceous aggregates from an urban aerosol. Environmental Science and Technology 27, 539–547.

Kittelson, D.B., 1998. Engines and nanoparticles: a review. Journal of Aerosol Science 29, 575–588.

MacKenzie, R.C., 1970. Differential Thermal Analysis, vol. 1. Academic Press, London.

Mitchell, R., Gu, J.D., 2000. Changes in biofilm microflora of limestone caused by atmospheric pollutants. International Biodeterioration & Biodegradation 46, 299–303.

Mirwald, P.W., Kraus, K., Wolf, A., 1988. Stone deterioration at the Cathedral of Cologne. Durability of Building Materials 5, 549–570.

Monna, F., Lancelot, J., Croudace, I.W., Cundy, A.B., Lewis, J.T., 1997. Pb isotopic composition of airborne particulate matter from France and Southern United Kingdom: implications for Pb pollution sources in urban areas. Environmental Science and Technology 31, 2277–2286.

Moropoulou, A., Polikreti, K., Ruf, V., Deodatis, G., 2003. San Francisco Monastery, Quito, Equador: characterization of building materials, damage assessment and conservation considerations. Journal of Cultural Heritage 4, 101–108.

Murr, L.E., Bang, J.J., 2003. Electron microscope comparisons of fine and ultra-fine carbonaceous and non-carbonaceous, airborne particulates. Atmospheric Environment 37, 4795–4806.

Nguyen, T.H., Brown, R.A., Ball, W.P., 2004. An evaluation of thermal resistance as a measure of black carbon content in diesel soot, wood char, and sediment. Organic Chemistry 35, 217–234.

Novakov, T., Chang, S.G., Harker, A.B., 1974. Sulfates as pollution particulates: catalytic formation on carbon (soot) particles. Science 186, 259–261.

Rodriguez-Navarro, C., Sebastian, E., 1996. Role of particulate matter from vehicle exhaust on porous building stones (limestone) sulfation. Science of the Total Environment 187, 79–91.

Rodriguez-Navarro, C., Doehne, E., 1999. Salt weathering: influence of evaporation rate, supersaturation and crystallization pattern. Earth Surface Processes and Landforms 24, 191–209.

Ross, M., McGee, E.S., Ross, D.R., 1989. Chemical and mineralogical effects of acid deposition on Shelburne marble and Salem limestone test samples placed at four NAPAP weather-monitoring sites. American Mineralogist 74, 367–383.

Sabbioni, C., Zappia, G., 1992. Atmospheric-derived element tracers on damaged stone. Atmospheric Environment 126, 35–48.

Sabbioni, C., Zappia, G., Gobbi, G., 1996. Carbonaceous particles and stone damage in a laboratory exposure system. Journal of Geophysical Research-Atmospheres 101, 19621–19627.

Schiavon, N., Chiavari, G., Schiavon, G., Fabbri, D., 1995. Nature and decay effects of urban soiling on granitic building stones. Science of the Total Environment 167, 87–101.

Schiavon, N., Zhou, L., 1996. Magnetic, chemical, and microscopical characterization of urban soiling on historical monuments. Environmental Science and Technology 30, 3624–3629.

Schiavon, N., 2000. Granitic building stone decay in an urban environment: a case of authigenic kaolinite formation by heterogeneous sulfur dioxide attack. In: Fassina, V. (Ed.), Ninth International Congress on Deterioration and Conservation of Stone. Venice, pp. 411–421.

Simão, J., 2003. Rochas Igneas Como Pedra Ornamental. Causas, Condicionantes e Mecanismos de Alteração. Implicações Tecnológicas. Ph.D. Thesis, Universidade Nova de Lisboa, Caparica, Portugal.

Smith, B.J., Magee, R.W., Whalley, W.B., 1993. Weathering of granite in a polluted environment: Budapest. In: Vicente, A., Ballesteros, E., Rives-Amau, V. (Eds.), Alteration of Granites and Similar Rocks used as Building Materials. C.S.I.C., Madrid, pp. 159–162.

Smith, B.J., Magee, R.W., 1990. Granite weathering in an urban environment: an example from Rio de Janeiro. Singapore Journal of Tropical Geography 2, 143–153.

Tambe, S., Gauri, K.L., Li, S., Cobourn, W.G., 1991. Kinetic study of SO_2 reaction with dolomite. Environmental Science and Technology 25, 2071–2075.

Tole, M.P., Lasaga, A.C., Pantano, C., White, W.B., 1986. The kinetics of dissolution of nepheline ($NaAlSiO_4$). Geochimica et Cosmochimica Acta 50, 379–392.

Wilson, M.J., 2004. Weathering of the primary rock-forming minerals: processes, products and rates. Clay Minerals 39, 233–266.

Xie, R.K., Seip, H.M., Leinum, J.R., Winje, T., Xiao, J.S., 2005. Chemical characterization of individual particles (PM10) from ambient air in Guiyang City, China. Science of the Total Environment 343, 261–272.

Zappia, G., Sabbioni, C., Gobbi, G., 1993. Non-carbonate carbon content on black and white areas of damaged stone monuments. Atmospheric Environment 27A, 1117–1121.

Zinbo, M., Korniski, T.J., Weir, J.E., 1993. Thermogravimetry of filter-borne gasoline engine-out particulates. Thermochimica Acta 226, 221–228.